PAPER

Check for updates

Numerical modeling investigations of the impact of a thin p-type cocatalyst modifier on an n-type photon absorber for unbiased overall solar water splitting†

HanHsuan Huang, Kesiuke Obata, Fuminao Kishimoto [iD] and
Kazuhiro Takanabe [iD] *

Surface modifications of semiconductor photoelectrodes are often introduced to enhance charge separation and reaction kinetics during solar-driven water splitting. Examples include the formation of n–n heterojunctions and the deposition of electrocatalyst layers. The internal electric field in a p–n junction is expected to be stronger than that in an n–n junction, and several studies have used p-type semiconducting electrocatalyst decoration to improve the overall performance of water splitting. However, a design guideline for the p-type modification layer has not been clearly reported. Therefore, we numerically investigated the impact of a thin p-type modification layer on the photoelectrochemical performance of an n-type photoanode. The key parameters were varied in simulations, including the band position, dopant densities, thickness of the p-type layer, and the dopant densities in the n-type region. Our numerical simulations show that the depletion depths in the p-type modification layer and n-type photon absorber are the key characteristics that need to be tuned, which is mainly achieved by controlling the dopant densities. This work also discusses the critical distinction of a p–n heterojunction compared to an n–n heterojunction photoanode.

Introduction

There are concerns about the depletion of fossil fuels, the increase in global energy demands, and environmental pollution. Therefore, recent research efforts have been dedicated to exploring green and clean energy sources in order to develop a sustainable society. Solar energy is the most abundant and promising renewable energy resource available. However, sunlight has problems related to seasonal and daily intermittency and weather. As such, the conversion of solar energy into a storable energy, such as chemical energy, is a goal for the implementation of renewable energy sources.

Several methods are being developed to store the electricity produced from photovoltaics, such as batteries, hydrogen production by water electrolysis, *etc.* Hydrogen is one energy carrier that can be easily stored, transferred, and used as a feedstock for chemical processes. Among the various approaches for solar energy conversion toward hydrogen, solar-driven

photoelectrochemical (PEC) water splitting is a promising method to produce clean and sustainable hydrogen because of its simplicity and compactness.[1–8] For commercial application, the present impediment of this technology is reaching a sufficient value ($\sim 10\%$) of solar-to-hydrogen (STH) energy conversion efficiency in a scalable manner.[9–12]

PEC cells basically consist of either a semiconductor photoanode or photocathode, which is immersed in an electrolyte. The oxygen evolution reaction (OER) and hydrogen evolution reaction (HER) take place on the anode and the cathode, respectively, using the excited carriers under solar irradiation. An appropriate band gap structure is the primary condition to achieving overall unbiased water splitting. The conduction band minimum (CBM) position needs to be more negative than the hydrogen evolution potential, and the valence band maximum (VBM) has to be more positive than the oxygen evolution potential.

Although STH efficiency above 10% is predicted based on the band gap,[13,14] the measured efficiency is often limited due to fast charge recombination, which is a detrimental process in the photoelectrochemical reaction. In addition to the charge separation, the sluggish kinetics of the OER is another challenge. Electron transfer between the semiconductor and electrolyte competes with the recombination of electrons and holes.

Department of Chemical System Engineering, School of Engineering, University of Tokyo, 7-3-1 Hongo, Bunkyo-ku, Tokyo, 113-8656, Japan.
E-mail: takanabe@chemsys.t.u-tokyo.ac.jp

Recombination occurs when the lifetime of the holes is shorter than the charge transfer kinetics or when there is no driving force to separate the charged carriers. Studies on the properties of photoanode materials and improvement strategies are necessary to prevent this charge recombination.

To overcome these limitations, the deposition of an OER co-catalyst on a nano-structured n-type photon absorber is frequently applied to extract the excited minority carriers and move them toward the OER co-catalyst. Thin layers or islands of catalysts are often applied to avoid parasitic light absorption.[15–17] There are catalysts which behave like metal, such as IrO_x and transition metal pnictide pre-catalysts.[18] The interfacial physics between a semiconductor and metallic catalyst have been investigated.[19,20] However, the conductivities of commonly used transition metal (oxy)hydroxides are reported to be 10^{-5}–10^{-2} S cm^{-1},[21,22] which is in the range of a semiconductor. Constructing a heterojunction has been proven to be an efficient and convenient method to enhance the separation of excited carriers. For example, an n–n heterojunction can result in a built-in electric field at the interface, which works as a driving force to promote charge separation.[23] On the other hand, the built-in electric field is expected to be stronger in a p–n junction because the Fermi levels in p- and n-type semiconductors are located close to the valence and the conduction bands, respectively. Therefore, fine tuning of the p–n heterojunction could be an effective approach to separate photo-generated carriers, which could enhance the photoelectrochemical activity. For example, Xie et al. deposited p-type NiO nanoparticles that act as island-like OER catalysts on a Mo-doped $BiVO_4$ nanobelt photoanode, which improved the separation of the photoexcited carriers through the formation of a p–n heterojunction.[24] Yi et al. fabricated p–n heterojunction nanostructure arrays composed of p-type Co_3O_4 islands and n-type Ti:Fe_2O_3 nanorods.[25] This kind of island-like structure can induce a unique effect on semiconductors like pinch-off.[26–28] However, direct contact between semiconductors and aqueous solutions may lead to deactivation due to self-photooxidation. For example, a Ta_3N_5 photoanode with a uniform catalyst layer was reported to show better stability compared to the one with a non-uniform layer.[29] However, a design guideline for thin p-type modification layers has not been clearly reported yet.

Tantalum-based semiconductors such as TaON,[30–36] Ta_2O,[37,38] and $LaTaN_2$[39,40] can satisfy most of the requirements of photocatalysts. Domen et al. introduced a new class of nitride semiconductors and found that tantalum nitride (Ta_3N_5) was the best candidate for PEC water oxidation that satisfies the thermodynamic requirements.[41–44] Moreover, its band gap is 2.1 eV, which means it can absorb visible light over a wide range up to approximately 600 nm, and it has a theoretical current density of 12.4 mA cm^{-2}.[45] However, the fast charge recombination is an obstacle that needs to be overcome.

Although multiple strategies are reported to enhance the photoelectrocatalytic performance of Ta_3N_5,[46–51] the construction of a heterojunction would be the most effective way.[52–54] For example, Ta_3N_5-based n–n heterojunctions have been developed by many groups.[48,55–57] Recently, our group reported a guideline for the design of Ta_3N_5-based n–n heterojunctions.[58] However, there is little research on Ta_3N_5-based p–n heterojunctions.[59,60]

This study investigates the numerical modeling of the photoanodic performance of a p–n heterojunction. The heterojunction is composed of an n-type photon absorber and p-type cocatalyst modification layer, which forms a Schottky junction with the electrolyte. Ta_3N_5 was selected as a model n-type photon absorber. We discuss several crucial parameters, including the band position, dopant densities, and thickness of the p-type modification layer to achieve zero-bias overall water splitting at a high photocurrent density. The results were compared with those of a previously established n–n heterojunction.

Models

Simulations were performed using COMSOL Multiphysics version 5.5 with a finite element method (FEM) to evaluate the band structures, charge density, and resulting current-potential curve in the photoelectrochemical systems. The element size of the physics control mesh feature was automatically set at a finer level. Several equations were applied in the entire model for the simulation, such as Poisson's equation (eqn (1)):

$$\nabla \cdot (\nabla \phi) = -\frac{q}{\varepsilon_0 \varepsilon_r}\left(p - n + N_d^+ - N_a^-\right) \quad (1)$$

where ϕ, q, ε_0, ε_r, N_d^+, and N_a^- are the electrostatic potential, electronic charge, electrical permittivity of free space, relative dielectric permittivity, positive donor, and negative acceptor densities in the semiconductor, respectively. The drift-diffusion and continuity equations are shown below:

$$\frac{\partial n}{\partial t} = \frac{1}{q}\nabla \cdot J_n + G_n(x) - R_n(x) \quad (2)$$

$$\frac{\partial p}{\partial t} = \frac{1}{q}\nabla \cdot J_p + G_p(x) - R_p(x) \quad (3)$$

$$\nabla \cdot (J_n + J_p) = 0 \quad (4)$$

$$J_n = qn\mu_n E + \mu_n k_B T \nabla n \quad (5)$$

$$J_p = qp\mu_p E + \mu_p k_B T \nabla p \quad (6)$$

where n and p are the electron and hole densities. J_n and J_p are the total electron and hole current densities due to the electric field E and the concentration gradient ∇n or ∇p. $G_{n,p}(x)$ and $R_{n,p}(x)$ represent the generation and recombination or annihilation rate of the electrons and holes at the depth x in the n-type photon absorber, respectively. k_B, T, and $\mu_{n,p}$ are Boltzmann's constant, the temperature, and the mobility of charge carriers, respectively. Fermi–Dirac statistics were applied for the calculations of the (quasi-) Fermi-energy level of electrons and holes as well.
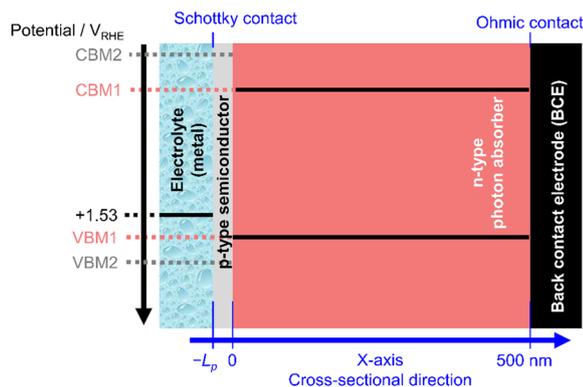
Fig. 1 Geometric model and electronic structure of the p–n junction photoanode composed of a p-type modification layer and an n-type photon absorber. The interface at the p-type modification layer/electrolyte and the n-type photon absorber/back contact are assumed to be Schottky and Ohmic contacts, respectively.

A schematic of the p–n heterojunction applied in this study is shown in Fig. 1. It is composed of a p-type semiconductor modification layer and an n-type photon absorber. The thickness of the p-type modification layer and the n-type photon absorber are L_p (variable) and 500 nm, respectively. The interface of the modification layer and electrolyte is assumed to be Schottky contact, whereas the interface of the photon absorber and metal back contact electrode (BCE) is set as the Ohmic contact.

Incident light is introduced from the electrolyte and absorbed in only the n-type photon absorber. The parasitic light absorption in the modification layer is ignored. According to the Lambert–Beer law, the following equation determines the charge generation rate:

$$G_n(x) = G_p(x) = P_0 \alpha \, \exp(-\alpha x) \tag{7}$$

where P_0 is the density of incident photon flux, and a is the absorption coefficient.

In this model, Shockley–Read–Hall (SRH) recombination that takes place via defect levels in the band gap was assumed to occur in only the photon absorber. The defect level is assumed to be located in the middle of the band gap. The recombination rate is expressed by the following equations:

$$R_n(x) = R_p(x) = \frac{n(x)p(x) - \gamma_n \gamma_p n_{i,\text{eff}}^2}{\tau_p n(x) + \tau_n p(x)} \tag{8}$$

$$n_{i,\text{eff}} = \sqrt{N_C N_V} \exp\left(-\frac{E_g}{2k_B T}\right) \tag{9}$$

γ_n and γ_p are parameters that represent the degree of degeneracy of electrons and holes. N_c and N_v are the effective density of states in the conduction band and valence band, respectively, and E_g is the energy band gap.

In the simulation, the electrolyte was assumed to be metallic with a constant Fermi level. Considering the common overpotential during the OER (around 0.3 V at 10 mA cm^{-2}),[18] its Fermi level was tentatively set to 1.53 V vs. reversible hydrogen electrode (RHE). We believe that the assumption of the constant overpotential is reasonable because our current density range studied was below 10 mA cm^{-2} and because Tafel slopes of these catalysts are often reported to be 40–80 mV dec^{-1},[18] which is not huge in our comparisons.

At this Schottky contact between the metal and p-type semiconductor, the electron and hole currents are determined by the carriers that overcome this barrier due to their thermal energy according to Fermi–Dirac distribution (i.e., thermionic emission current). The following equations determine the current flowing through the Schottky contact:

$$\nu_{n,p} = \frac{A_{n,p} T^2}{q N_{C,V}} \tag{10}$$

$$A_{n,p} = \frac{4\pi m_{n,p} m_0 q k_B^2}{h^3} \tag{11}$$

$$J = J_p + J_n \tag{12}$$

$$J_p = q\nu_p(p - p_0) \tag{13}$$

$$J_n = -q\nu_n(n - n_0) \tag{14}$$

where $\nu_{n,p}$, $A_{n,p}$, and J are the velocity of carriers, Richardson constant, and total current density, respectively. m_0, m_n, and m_p are the electron mass and effective mass ratio of electrons and holes, respectively.

From the bulk neutral region toward the junction, a narrow transition region appears. This region is called the space-charge region or, in some cases, the depletion region to be more specific, where electrons diffuse across the interface to combine with holes. The built-in potential, V_{bi}, represents the total of the electrostatic potential difference between the p- and n-type neutral regions at thermal equilibrium, where ψ_n and $|\psi_p|$ are the electrostatic potential of the n- and p-type neutral region, respectively. To estimate x_p and x_n, the width of the depletion region in the p- and n-type regions respectively, the following equations were considered:

$$V_{bi} = \psi_n + |\psi_p| \tag{15}$$

$$x_p = \sqrt{\frac{2\varepsilon_s}{q} \frac{N_d}{N_a} \frac{1}{N_a + N_d} (V_{bi})} \tag{16}$$

$$x_n = \sqrt{\frac{2\varepsilon_s}{q} \frac{N_a}{N_d} \frac{1}{N_a + N_d} (V_{bi})} \tag{17}$$

The light penetration depth in the n-type region, δ_n, is calculated by:

$$\delta_n = \frac{1}{\alpha} \tag{18}$$

Tables 1 and 2 show the parameters of n-type Ta$_3$N$_5$ and those of the p-type modification layer, respectively. The varied parameters are highlighted in bold. Physical constants are shown in Table 3. In this study, we defined the onset potential as the point where the current density reaches 0.05 mA cm^{-2}.

Table 1 List of material parameters of n-type photon absorber applied in the numerical simulations. These values were determined from the reported values of Ta$_3$N$_5$ photoelectrodes.[12,29,61–64] Parameters varied in this study are shown in bold

Symbol	Value	Unit	Description
CBM1	−0.34	V *versus* RHE (V$_{RHE}$)	Conduction band minimum
VBM1	+1.76	V *versus* RHE (V$_{RHE}$)	Valence band maximum
ε_r	17	—	Relative permittivity
E_g	2.1	eV	Band gap
c	4.1	eV	Electron affinity
N_v	1×10^{20}	cm^{-3}	Effective density of states in VB
N_c	1×10^{20}	cm^{-3}	Effective density of states in CB
μ_n	2	cm^2 V^{-1} s^{-1}	Electron mobility
μ_p	0.2	cm^2 V^{-1} s^{-1}	Hole mobility
N_d	**1×10^{19}**	**cm^{-3}**	**Donor density**
τ_n	2×10^{-9}	s	Electron lifetime
τ_p	2×10^{-9}	s	Hole lifetime
P_0	9×10^{20}	m^{-2} s^{-1}	Photon flux
α	6×10^6	m^{-1}	Absorption coefficient

Table 3 List of other physical constants and parameters

Symbol	Value	Unit	Description
h	6.62×10^{-34}	J s	Planck constant
k_B	1.3806×10^{-23}	J K^{-1}	Boltzmann constant
q	1.602×10^{-19}	C	Elementary charge
μ_0	9.1094×10^{-31}	kg	Electron mass
μ_n	1.9		Effective mass ratio of electron
m_p	3.4		Effective mass ratio of hole
T	298	K	Temperature in model

Semi-log JV curves which were taken from Fig. 5a, as an example, are shown in Fig. S1 (ESI†). Although the onset potential may shift *ca.* 100 mV when the defined current density is changed by one order of magnitude below 0.1 mA cm^{-2}, these curves are parallel, which means that the trend in the parametric study should be independent to the definition of the onset potential (below 0.1 mA cm^{-2}).

Results and discussion

Fig. 2a shows the energy levels of separated layers, the electrolyte, the p-type modification layer, and the n-type photon absorber. The parameters are $N_a = 1 \times 10^{19}$ cm^{-3}, $c = 3.3$ eV, VBM2 = 2.26 V_{RHE}, and $E_{g2} = 3.4$ eV in the p-type layer, and $N_d = 1 \times 10^{19}$ cm^{-3}, $c = 4.1$ eV, VBM2 = 1.76 V_{RHE}, and $E_g = 2.1$ eV in the n-type layer. After they make contact with each other (Fig. 2b), due to the difference in the Fermi-level in the contacting layers, the free electrons and holes will be transferred across two materials to recombine. This process results in the formation of the depletion region and the electric field at the interface due to the remaining donor and acceptor ions until it reaches an equilibrium where the Fermi-level attains to the same level. Downward and upward band bending from the right-side semiconductor appear at the Schottky interface and

p–n junction, respectively. The bending value depends on the difference between the valence band of the metal and the Fermi level in the p-type layer, which is 0.6 V_{RHE}, as well as the difference from the n-type to the p-type layer, which is 2.4 V_{RHE} in this example. Based on the predicted opposite bending, we performed a series of simulations to investigate the photoelectrochemical characteristics in the presence of the Schottky contact and the p–n junction.

Effects of the valence band position in the p-type modification layer

The valence band position in the p-type modification layer is expected to play an important role of guiding the holes from the bulk semiconductor to the electrolyte. The valence band position was varied to investigate the resulting current-potential curves and the band diagrams. The physical parameters of the n-type photon absorber were set as shown in Table 1. The valence band maximum of the p-type semiconducting modification layer, VBM2, was varied from +1.46 to +2.86 V_{RHE}, and the other parameters were set constant, as shown in Table 2.

In Fig. 3a, the VBM2 is varied from +2.06 to +2.46 V_{RHE}. The current-potential curve changes significantly in this range, which can be explained by the band diagrams. Fig. 3b summarizes the photoanodic performance in response to VBM2. When the value of VBM2 went beyond +2.46, a significant transition of the onset potential was observed. The valence band diagrams are shown in Fig. 3c. Obviously, both the Schottky contact and p–n junction contribute to the present heterojunction. The upward bending from the bulk semiconductor to the interface developed by the p–n junction can effectively suppress the excited carriers that recombine in the photon absorber. A V-shape band structure also appears at the

Table 2 List of default parameters in the surface modification layer of p-type semiconductors applied in the numerical simulations. The parameters varied in this study are shown in bold

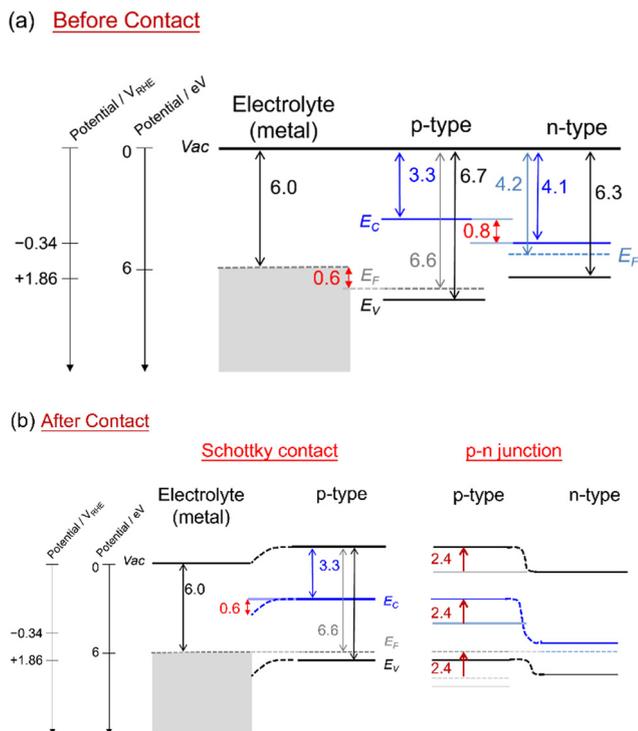| Symbol	Value	Unit	Description
L_p	**25**	**nm**	**Thickness of the modification layer**
CBM2	−1.14	V *versus* RHE (V$_{RHE}$)	Conduction band minimum
VBM2	**+2.26**	**V *versus* RHE (V$_{RHE}$)**	**Valence band maximum**
ε_{r2}	17	–	Relative permittivity
E_{g2}	**3.4**	**eV**	**Band gap**
c_2	3.3	eV	Electron affinity
N_v	1×10^{20}	cm^{-3}	Effective density of states in VB
N_c	1×10^{20}	cm^{-3}	Effective density of states in CB
μ_{n2}	2	cm^2 V^{-1} s^{-1}	Electron mobility
μ_{p2}	0.2	cm^2 V^{-1} s^{-1}	Hole mobility
N_a	**1×10^{19}**	**cm^{-3}**	**Acceptor density**

(a) Before Contact

(b) After Contact

Fig. 2 Band diagrams of the electrolyte (assumed to be metallic), p-type layer, and n-type layer (a) before and (b) after contact. Vac, E_C, E_V, and E_F represent the vacuum level, conduction band, valence band, and Fermi level, respectively.

heterointerface between the p-type and n-type layers. Its depth strongly depends on VBM2.

The huge gap (> 0.6 eV) might have blocked the photo-generated holes from transferring from the photon absorber to the modification layer at the highest VBM2 of 2.46 V_{RHE}. The gap was smaller when reducing VBM2, which allowed accumulated holes to pass through the interface. Overall, the relatively low VBM2 (below 2.2 V_{RHE}) is preferable for achieving unbiased water splitting.

Remarkably, although VBM2 is more positive than VBM1 (1.76 V_{RHE}), a clear photodiode characteristic was still obtained. To develop the present p–n junction with the OER catalyst layer, for example, the valence band position of NiO_x is reported to be 1.0 V_{RHE},[65] and Sun et al. successfully produced oxygen using p-type NiO_x as an OER catalyst on an n-Si photoanode.[66] In the present study, VBM2 was varied while CBM2 was maintained which means that the band gap in the p-type layer changes. The band gap in the p-type layer is 3.2–3.8 eV while that in the n-type layer is 2.1 eV, which suggests that parasitic light absorption by the modification layer can be ignored. However, a trade-off effect should be considered when the band gap of the p-type layer is comparable to that in the n-type layer.

Impact of the acceptor density in the p-type modification layer

The effect of N_a on the PEC performance was investigated. The donor density was fixed at 1×10^{19} cm^{-3}, as shown in Table 1, and N_a was varied from 1×10^{17} to 1×10^{19} cm^{-3}. The simulated
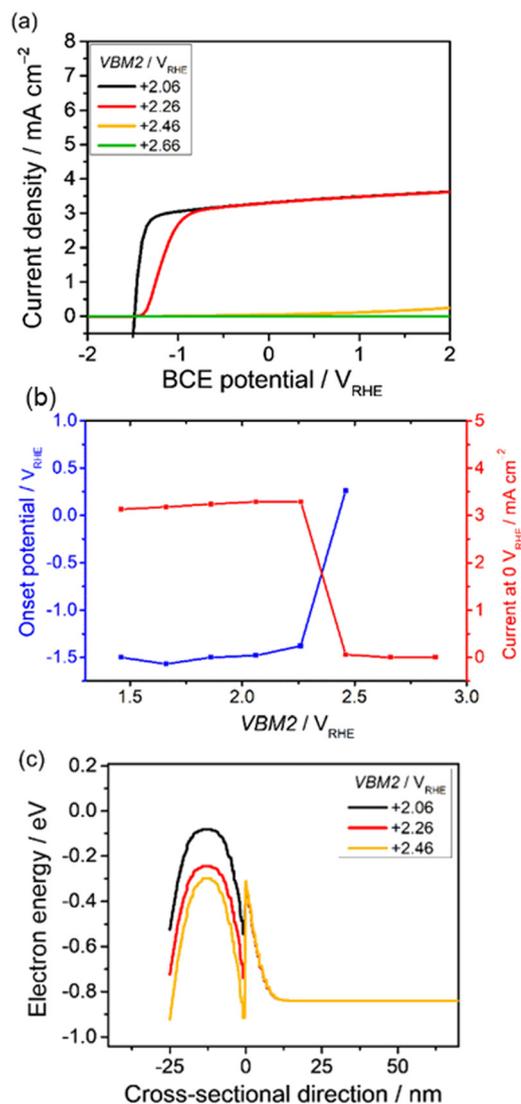

Fig. 3 (a) Current-potential curves of the p–n junction photoanode with varied VBM position in the p-type modification layer, VBM2, from +2.06 to +2.86 V_{RHE}. (b) The onset potential and the current density at 0 V_{RHE} with various VBM2. When VBM2 is above 2.5 V vs. RHE, the current density did not reach 0.05 mA cm^{-2}. (c) Extracted valence band diagram at -1.2 V_{RHE} with VBM2 varied from +2.06 to +2.46 V_{RHE}.

current-potential curves are shown in Fig. 4a, and the extracted current density at 0 V_{RHE} and the onset potential are shown in Fig. 4d. The current density remains almost constant, and the onset potential does not vary dramatically when the N_a concentration is below approximately 3×10^{18} cm^{-3}. In this range, the calculated depletion depth from eqn (16) and (17) in the p-type layer is much thicker than the setting value (25 nm). The result can be explained by the green curve in Fig. 4d and e, where the depletion in the p-type layer cannot form completely. This leads to a recombination loss mechanism, as shown by the high hole density in the n-type layer near the interface.

The current density at 0 V_{RHE} increases sharply at 3×10^{18} cm^{-3}, and the onset potential is negatively shifted by approximately 2.5 V vs. RHE when increasing N_a. Undeniably,
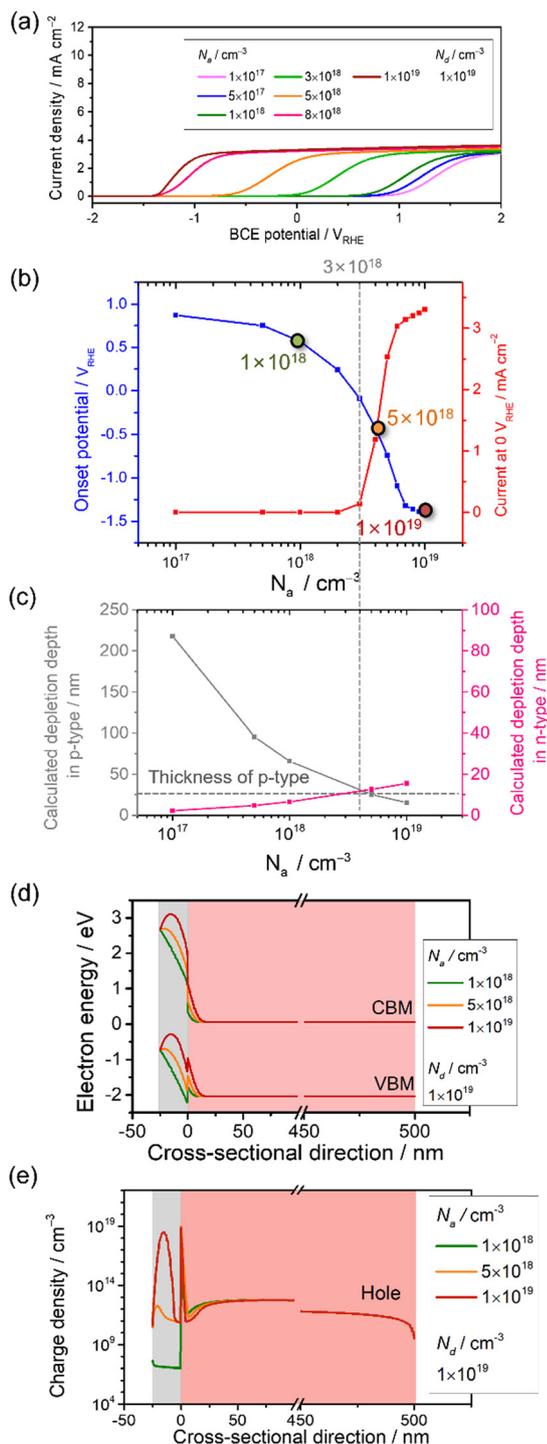
Fig. 4 Current-potential of a p–n junction photoanode with varied acceptor density in the p-type modification layer, N_a, from 1×10^{17} cm^{-3} to 1×10^{19} cm^{-3}. N_d is maintained at 1×10^{19} cm^{-3}. (b) Extracted onset potential and current density at 0 V_{RHE} with respect to N_a. (c) The depletion depth in the p-type region (grey) and n-type region (pink) with varied N_a estimated from eqn (16) and (17). (d) Energy band diagram and (e) charge density with N_a varied from 1×10^{18} cm^{-3} to 1×10^{19} cm^{-3} at 0 V_{RHE}.

a depletion region in the p-type modification layer is formed by both p–n junction and Schottky contact. Although the opposite

bending from the Schottky contact appears, increasing N_a reduces the depletion depth in the p-type layer coming from the p–n interface (Fig. 4c and d). In this critical section, the tendency starts to drastically change.

Lastly, the thickness of the depletion region in the p-type modification layer developed by the p–n junction becomes thin compared to the modification layer (25 nm). Hence, when N_a reaches 1×10^{19} cm^{-3}, the fully developed p–n junction forms a stronger electric field that drives the holes toward the electrolyte. The density distribution of minority holes along the cross-sectional direction (Fig. 4e) indicates that the hole density in the n-type layer near the interface decreases when increasing N_a, which means that the recombination loss mechanism is weakened.

V-shape traps are present at the interface between the p- and n-type layers due to the heterojunction (Fig. 4d), but their contribution seems to be minor as long as VBM2 is negative enough, as discussed in Section 3.1. OER catalyst modification layers are often deposited on semiconductors by dry or wet processes. Wet processes such as electrodeposition and spin coating naturally result in high doping concentrations. Considering the present results, wet processes seem to be preferable to dry vacuum processes, which result in high-quality films.

Influence of donor density in the n-type photon absorber

The effect of the donor density in the photon absorber, N_d, was next investigated with different values of N_a to see the influence on the current-potential curves. The other parameters in the p-type modification layer were maintained as shown in Table 2. Firstly, N_d was varied from 1×10^{17} to 1×10^{19} cm^{-3}, and N_a was fixed at 1×10^{19} cm^{-3}. As shown in Fig. 5a, the current density at 0 V_{RHE} decreases from 9 to 3 mA cm^{-2} when increasing N_d. Secondly, with relatively low N_a (5×10^{17} cm^{-3}), the current density decreases from 3 to 0 mA cm^{-2} (Fig. 5b). Fig. 5c shows the extracted onset potential values and the current densities at 0 V_{RHE} from the current–potential curves. When the p–n junction is fully developed in the modification layer in the range of N_d variation (Fig. 5d), the onset potential remained constant. When N_a and N_d are at comparable levels, the onset potential shifts when changing N_d because the depletion depth in the p-type region also varies with N_d (Fig. 5e).

Considering the light penetration depth of 170 nm, a relatively low donor density is preferable because the width of the depletion region in the n-type photon absorber is thick enough to cover the light penetration depth (Fig. 5e). Therefore, excited charge carriers can be effectively migrated by the electric field in the depletion layer. Enlargement of the depletion layer in the photon absorber can also be found in the simulated band diagram (Fig. 5d and f). Therefore, for an n-type photon absorber, high quality with a low dopant concentration is required since the donor density in the photon absorber strongly affects the attainable photocurrent.

Donor density determines the resistivity in the bulk n-type region and the resultant ohmic voltage loss. Using the parameters in Table 1 and the donor density of 1×10^{17} cm^{-3}, the
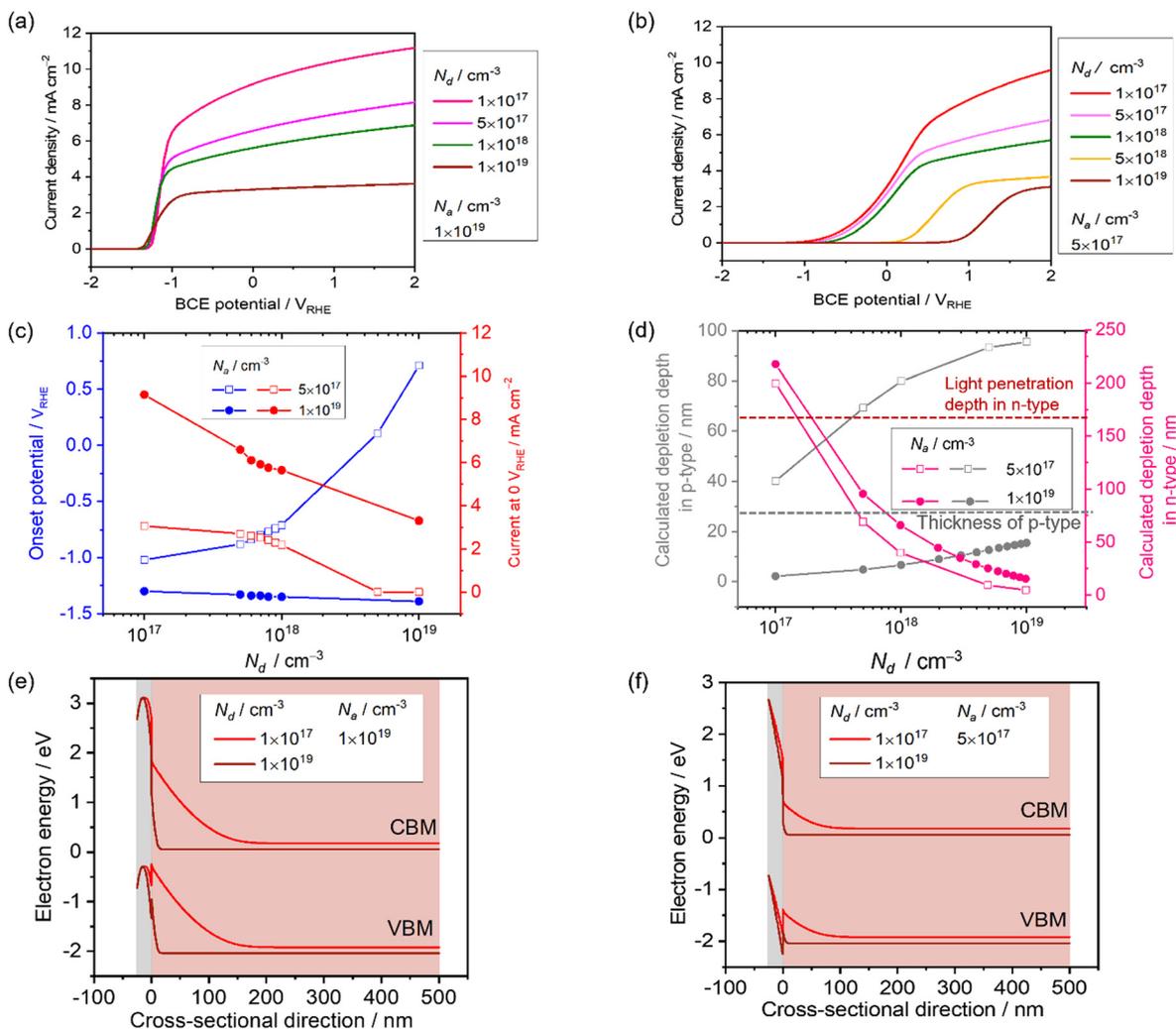
Fig. 5 (a) and (b) Current-potential of the p–n junction photoanode with varied donor density in the n-type photoanode (N_d) from 1×10^{17} cm^{-3} to 1×10^{19} cm^{-3}. (a) $N_a = 1 \times 10^{19}$ cm^{-3}, and (b) $N_a = 5 \times 10^{17}$ cm^{-3}. (c) Effect of N_d on the onset potential and current density at 0 V_{RHE}. (e) The width of the depletion region in the p-type region (gray) and n-type region (pink) with varied N_d and N_a. Energy band diagram with N_d varied from 1×10^{17} cm^{-3} to 1×10^{19} cm^{-3} at 0 V_{RHE}, (d) $N_a = 1 \times 10^{19}$ cm^{-3}, and (f) $N_a = 5 \times 10^{17}$ cm^{-3}.

resistance and the ohmic voltage loss were estimated to be 1.6 mΩ and 1.6×10^{-2} mV, respectively, at 10 mA cm^{-2} with an area of 1 cm^2 and a thickness of 500 nm. This ohmic voltage loss is negligible in our JV curves, which indicates that the conductivity and the thickness in the bulk n-type region do not play a major role in our simulation.

Consideration of the modification layer thickness with respect to the depletion depth

The thickness of the p-type modification layer was varied from 10 to 25 nm with fixed N_a (1×10^{19} cm^{-3}). N_d is 1×10^{19} cm^{-3} and 1×10^{18} cm^{-3} in Fig. 6a and b, respectively. As Fig. 6c shows, the onset potential is negatively shifted when the thickness increases. When the donor density is reduced to 1×10^{18} cm^{-3}, a constant onset potential was obtained because the thickness of the depletion depth in the p-type region (6.6 nm) is less than the simulated thickness range, which results in a fully developed p–n junction (Fig. 6d). Therefore,

the thickness of the modification layer should be carefully designed to cover the depletion depth, which is determined by the dopant densities. A thick modification layer would result in parasitic light absorption, which is not considered in the present study. The trade-off highlights the severe restriction on the catalyst modification, which is unique compared to p–n photovoltaic or buried p–n junction photoelectrodes.

Comparison between the p–n junction and n–n junction

The tendencies on the varied parameters were compared between the p–n junction and an n–n junction,[58] as shown in Fig. 7. The effects of the modification layer thickness in these two junctions are opposite. For the n–n heterojunction, favorable upward bending was predicted at the heterointerface in the thinnest one (10 nm), while unfavorable bending appeared at the n–n interface with a thicker layer. The critical distinction from the n–n junction is the formation of a depletion layer in the p–n junction, which results in the development of an
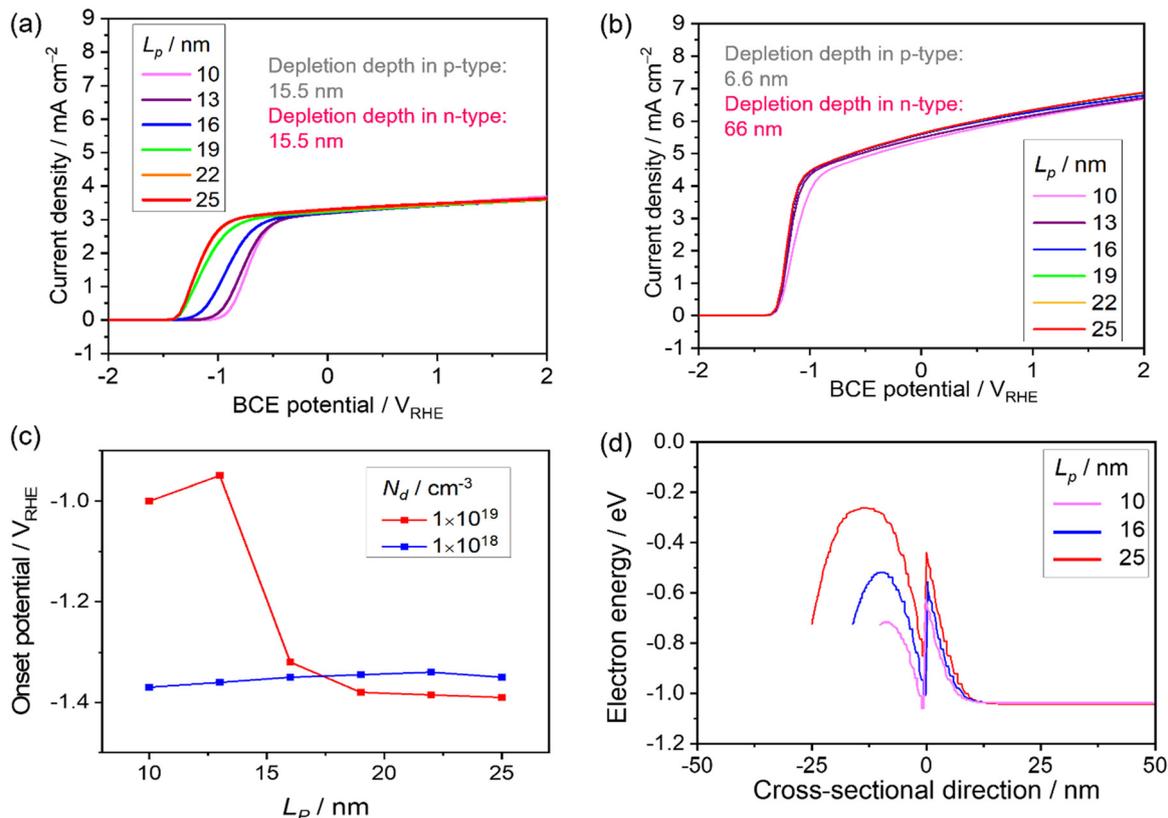
Fig. 6 Current-potential of the p–n junction photoanode with varied thickness in the p-type modification layer (L_p) from 10–25 nm at N_a = 1×10^{19} cm^{-3}: (a) $N_d = 1 \times 10^{19}$ cm^{-3}, and (b) $N_d = 1 \times 10^{18}$ cm^{-3}. (c) Effect of L_p at $N_d = 1 \times 10^{19}$ cm^{-3} (red) and 1×10^{18} cm^{-3} (blue) on the onset potential. (d) Extracted valence band diagram with L_p from 10 to 25 nm under -0.6 V_{RHE} with $N_d = N_a = 1 \times 10^{19}$ cm^{-3}.
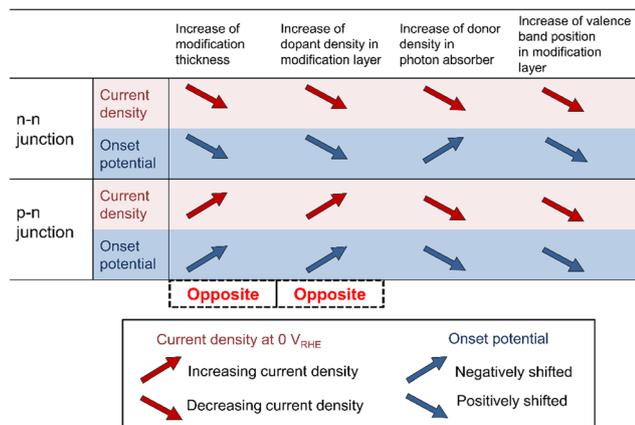

Fig. 7 Comparison of the current density at 0 V_{RHE} and onset potential between the n–n junction[58] and p–n junction.

electric field. Therefore, the p-type modification layer needs to be thick enough to fully develop the depletion layer.

The effects of the dopant density in the modification layer in these two situations are opposite as well. From the charge density distribution in the n–n heterojunction, an increase in the hole (minority carrier) concentration was observed in the n-type photon absorber near the interface with increasing donor density in the modification layer, which enhanced the electron-hole recombination. The fully developed p–n junction can contribute a stronger electric field to drive the holes towards the electrolyte. Increasing N_a can reduce the depletion depth in the p-type layer at the p–n interface. Thus, a decrease in the hole concentration can be observed in the n-type photon absorber with increasing acceptor density of the modification layer, leading to the suppression of the recombination.

A lower donor density in the photon absorber is obviously preferable to improve the attainable photocurrent because the thickness of the depletion region in the photon absorber is increased to cover the light penetration depth. This results in the effective migration of the excited carriers due to the electric field. However, the effect of donor density in the photon absorber shows a trade-off relationship between the onset potential and the current density in the n–n heterojunction, indicating that the donor density needs to be carefully optimized for the target operation. A lower doner density is preferable in the p–n heterojunction because it helps the formation of the fully developed p–n junction in the thin layer. Lastly, the effects of valence band position in the modification layer have the same tendency. Relatively low VBM2 is preferable because the favorable band bending appears to improve the performance.

The current ideal modeling of the semiconductor junction predicts the p-type modification layer to be a better candidate

rather than n-type modification for enhancing the photoelectrocatalytic performance because of the lower onset potential of the p–n junction. Theoretically, the built-in electric field in a p–n junction is stronger than the n–n junction, which is consistent with this result. These studies should be able to provide a quantitative guideline for establishing thin layer modification of the photoelectrode.

Conclusions

In this study, we used classical semiconductor theory to demonstrate a series of simulations to enhance the performance of an n-type photoanode covered with a thin p-type modification layer. Several pivotal parameters were analyzed to provide a guideline to achieve a higher photocurrent density without any bias, including the valence band position, dopant densities in both the p-type modification layer and n-type photon absorber, and the thickness of the modification layer. Also, we investigated the difference between the p–n junction and an n–n heterojunction. To design an ideal p–n heterojunction, the depletion depths in the p-type modification layer and n-type photon absorber must carefully be tuned with respect to the thickness of the modification layer and the light penetration depth by controlling their dopant densities. Furthermore, VBM2 should be below 0.44 V_{RHE} from the valence band position in the n-type absorber. Undeniably, more conditions should be considered for the photoanode design model since the model was applied using the classical theory, and we neglected some realistic potential-dependent reaction kinetics, parasitic light absorption, and the other factors. However, this study could still provide an idea of how to improve a photoanode covered with a thin layer of p-type OER electrocatalysts.

Author contributions

Conceptualization, F. K. and K. T.; methodology, H. H. and K. O.; investigation, H. H., F. K. and K. O.; writing – original draft, H. H.; writing – review & editing, H. H., K. O., F. K., and K. T.; supervision, K. T.; funding acquisition, K. T.

Conflicts of interest

There are no conflicts to declare.

Acknowledgements

References

1 J. Brillet, M. Comuz, F. LeFormal, J. H. Yum, M. Grätzel and K. Sivula, *J. Mater. Res.*, 2010, **25**, 17–24.

2 Q. Wang, T. Hisatomi, Y. Suzuki, Z. Pan, J. Seo, M. Katayama, T. Minegishi, H. Nishiyama, T. Takata, K. Seki, A. Kudo, T. Yamada and K. Domen, *J. Am. Chem. Soc.*, 2017, **139**, 1675–1683.

3 S. Chen, T. Takata and K. Domen, *Nat. Rev. Mater*, 2017, **2**, 17050.

4 T. Hisatomi, J. Kubota and K. Domen, *Chem. Soc. Rev.*, 2014, **43**, 7520–7535.

5 X. Chen, S. Shen, L. Guo and S. S. Mao, *Chem. Rev.*, 2010, **110**, 6503–6570.

6 M. G. Walter, E. L. Warren, J. R. McKone, S. W. Boettcher, Q. Mi, E. A. Santori and N. S. Lewis, *Chem. Rev.*, 2010, **110**, 6446–6473.

7 L. Finegold and J. L. Cude, *Nature*, 1972, **238**, 38–40.

8 S. S. Mao, S. Shen and L. Guo, *Prog. Nat. Sci. Mater. Int*, 2012, **22**, 522–534.

9 W. H. Cheng, M. H. Richter, M. M. May, J. Ohlmann, D. Lackner, F. Dimroth, T. Hannappel, H. A. Atwater and H. J. Lewerenz, *ACS Energy Lett*, 2018, **3**, 1795–1800.

10 Y. Pihosh, I. Turkevych, K. Mawatari, J. Uemura, Y. Kazoe, S. Kosar, K. Makita, T. Sugaya, T. Matsui, D. Fujita, M. Tosa, M. Kondo and T. Kitamori, *Sci. Rep*, 2015, **5**, 11141.

11 B. A. Pinaud, J. D. Benck, L. C. Seitz, A. J. Forman, Z. Chen, T. G. Deutsch, B. D. James, K. N. Baum, G. N. Baum, S. Ardo, H. Wang, E. Miller and T. F. Jaramillo, *Energy Environ. Sci.*, 2013, **6**, 1983–2002.

12 T. Higashi, H. Nishiyama, Y. Suzuki, Y. Sasaki, T. Hisatomi, M. Katayama, T. Minegishi, K. Seki, T. Yamada and K. Domen, *Angew. Chem., Int. Ed.*, 2019, **58**, 2300–2304.

13 S. Hu, C. Xiang, S. Haussener, A. D. Berger and N. S. Lewis, *Energy Environ. Sci.*, 2013, **6**, 2984–2993.

14 K. T. Fountaine, H. J. Lewerenz and H. A. Atwater, *Nat. Commun.*, 2016, **7**, 13706.

15 Y. Pihosh, T. Minegishi, V. Nandal, T. Higashi, M. Katayama, T. Yamada, Y. Sasaki, K. Seki, Y. Suzuki, M. Nakabayashi, M. Sugiyama and K. Domen, *Energy Environ. Sci.*, 2020, **13**, 1519–1530.

16 W. Smith, A. Wolcott, R. C. Fitzmorris, J. Z. Zhang and Y. Zhao, *J. Mater. Chem.*, 2011, **21**, 10792–10800.

17 Y. Pihosh, V. Nandal, T. Minegishi, M. Katayama, T. Yamada, K. Seki, M. Sugiyama and K. Domen, *ACS Energy Lett*, 2020, **5**, 2492–2497.

18 N. T. Suen, S. F. Hung, Q. Quan, N. Zhang, Y. J. Xu and H. M. Chen, *Chem. Soc. Rev.*, 2017, **46**, 337–365.

19 T. J. Mills, F. Lin and S. W. Boettcher, *Phys. Rev. Lett.*, 2014, **112**, 148304.

20 M. R. Nellist, F. A. L. Laskowski, F. Lin, T. J. Mills and S. W. Boettcher, *Acc. Chem. Res.*, 2016, **49**, 733–740.

21 M. S. Burke, M. G. Kast, L. Trotochaud, A. M. Smith and S. W. Boettcher, *J. Am. Chem. Soc.*, 2015, **137**, 3638–3648.

22 D. Maity, K. Karmakar and K. Mandal, *J. Alloys Compd.*, 2019, **791**, 739–746.

23 M. S. Burke, S. Zou, L. J. Enman, J. E. Kellon, C. A. Gabor, E. Pledger and S. W. Boettcher, *J. Phys. Chem. Lett.*, 2015, **6**, 3737–3742.

24 S. Xie, T. Zhai, Y. Zhu, W. Li, R. Qiu, Y. Tong and X. Lu, *Int. J. Hydrogen Energy*, 2014, **39**, 4820–4827.

25 S. S. Yi, B. R. Wulan, J. M. Yan and Q. Jiang, *Adv. Funct. Mater.*, 2019, **29**, 1801902.

26 F. A. L. Laskowski, M. R. Nellist, R. Venkatkarthick and S. W. Boettcher, *Energy Environ. Sci.*, 2017, **10**, 570–579.

27 F. A. L. Laskowski, S. Z. Oener, M. R. Nellist, A. M. Gordon, D. C. Bain, J. L. Fehrs and S. W. Boettcher, *Nat. Mater.*, 2020, **19**, 69–76.

28 A. T. Garcia-Esparza and K. Takanabe, *J. Mater. Chem. A*, 2016, **4**, 2894–2908.

29 Y. Kawase, T. Higashi, M. Katayama, K. Domen and K. Takanabe, *ACS Appl. Mater. Interfaces*, 2021, **13**, 16317–16325.

30 S. S. Gujral, A. N. Simonov, M. Higashi, X. Y. Fang, R. Abe and L. Spiccia, *ACS Catal.*, 2016, **6**, 3404–3417.

31 S. Li, C. Wang, M. Cai, F. Yang, Y. Liu, J. Chen, P. Zhang, X. Li and X. Chen, *Chem. Eng. J.*, 2022, **428**, 131158.

32 Z. Wang, J. Hou, S. Jiao, K. Huang and H. Zhu, *J. Mater. Chem.*, 2012, **22**, 21972–21978.

33 H. Jiang, W. Zhang, S. Zang and W. Zhang, *Int. J. Hydrogen Energy*, 2019, **44**, 24218–24227.

34 L. Pei, T. Li, Y. Yuan, T. Yang, J. Zhong, Z. Ji, S. Yan and Z. Zou, *Chem. Commun.*, 2019, **55**, 11754–11757.

35 M. Hara, G. Hitoki, T. Takata, J. N. Kondo, H. Kobayashi and K. Domen, *Catal. Today*, 2003, **78**, 555–560.

36 S. Wang, Z. Li, Y. Guan, L. Lu, Z. Shi, P. Weng, S. Yan and Z. Zou, *Appl. Catal. B Environ.*, 2019, **245**, 220–226.

37 H. Jiang, L. Feng, S. Zhu, X. Li and S. Zang, *Int. J. Hydrogen Energy*, 2021, **46**, 39855–39867.

38 H. Jiang, X. Li, S. Zang and W. Zhang, *J. Alloys Compd.*, 2021, **854**, 155328.

39 A. Yamakata, M. Kawaguchi, N. Nishimura, T. Minegishi, J. Kubota and K. Domen, *J. Phys. Chem. C*, 2014, **118**, 23897–23906.

40 X. Lu, A. Bandara, M. Katayama, A. Yamakata, J. Kubota and K. Domen, *J. Phys. Chem. C*, 2011, **115**, 23902–23907.

41 A. Ishikawa, T. Takata, J. N. Kondo, M. Hara and K. Domen, *J. Phys. Chem. B*, 2004, **108**, 11049–11053.

42 C. T. Ho, K. BinLow, R. F. Klie, K. Maeda, K. Domen, R. J. Meyer and P. T. Snee, *J. Phys. Chem. C*, 2011, **115**, 647–652.

43 D. Choi and P. N. Kumta, *J. Am. Ceram. Soc.*, 2007, **90**, 3113–3120.

44 V. Nandal, Y. Pihosh, T. Higashi, T. Minegishi, T. Yamada, K. Seki, M. Sugiyama and K. Domen, *Energy Environ. Sci.*, 2021, **14**, 4038–4047.

45 G. Hitoki, A. Ishikawa, T. Takata, J. N. Kondo, M. Hara and K. Domen, *Chem. Lett.*, 2002, 736–737.

46 M. Li, W. Luo, D. Cao, X. Zhao, Z. Li, T. Yu and Z. Zou, *Angew. Chem., Int. Ed.*, 2013, **52**, 11016–11020.

47 J. Fu and S. E. Skrabalak, *J. Mater. Chem. A*, 2016, **4**, 8451–8457.

48 Y. Jiang, P. Liu, Y. C. Chen, Z. Zhou, H. Yang, Y. Hong, F. Li, L. Ni, Y. Yan and D. H. Gregory, *Appl. Surf. Sci.*, 2017, **391**, 392–403.

49 R. Gao, S. Zhou, M. Chen and L. Wu, *J. Mater. Chem.*, 2011, **21**, 17087–17090.

50 S. Chen, Y. Qi, Q. Ding, Z. Li, J. Cui, F. Zhang and C. Li, *J. Catal.*, 2016, **339**, 77–83.

51 S. Grigorescu, B. Bärhausen, L. Wang, A. Mazare, J. E. Yoo, R. Hahn and P. Schmuki, *Electrochem. commun.*, 2015, **51**, 85–88.

52 X. Zhan, Z. Fang, B. Li, H. Zhang, L. Xu, H. Hou and W. Yang, *J. Mater. Chem. A*, 2021, **9**, 27084–27094.

53 H. Wang, L. Zhang, Z. Chen, J. Hu, S. Li, Z. Wang, J. Liu and X. Wang, *Chem. Soc. Rev.*, 2014, **43**, 5234–5244.

54 H. Li, Y. Zhou, W. Tu, J. Ye and Z. Zou, *Adv. Funct. Mater.*, 2015, **25**, 998–1013.

55 W. Zhang, H. Jiang, W. Zhang and S. Zang, *RSC Adv.*, 2020, **10**, 29424–29431.

56 W. P. Hsu, M. Mishra, W. S. Liu, C. Y. Su and T. P. Perng, *Appl. Catal. B Environ.*, 2017, **201**, 511–517.

57 P. Zhang, T. Wang and J. Gong, *Chem. Commun.*, 2016, **52**, 8806–8809.

58 K. Hatagami, F. Kishimoto, Y. Kawase, T. Higashi, V. Nandal, K. Seki and K. Takanabe, *Energy Technol.*, 2022, **10**, 2100570.

59 S. Li, S. Hu, K. Xu, W. Jiang, Y. Liu, Z. Leng and J. Liu, *J. Colloid Interface Sci.*, 2017, **504**, 561–569.

60 M. Liao, J. Feng, W. Luo, Z. Wang, J. Zhang, Z. Li, T. Yu and Z. Zou, *Adv. Funct. Mater.*, 2012, **22**, 3066–3074.

61 A. Ziani, E. Nurlaela, D. S. Dhawale, D. A. Silva, E. Alarousu, O. F. Mohammed and K. Takanabe, *Phys. Chem. Chem. Phys.*, 2015, **17**, 2670–2677.

62 E. Nurlaela, S. Ould-Chikh, M. Harb, S. DelGobbo, M. Aouine, E. Puzenat, P. Sautet, K. Domen, J. M. Basset and K. Takanabe, *Chem. Mater.*, 2014, **26**, 4812–4825.

63 H. Hajibabaei, O. Zandi and T. W. Hamann, *Chem. Sci.*, 2016, **7**, 6760–6767.

64 E. Nurlaela, Y. Sasaki, M. Nakabayashi, N. Shibata, T. Yamada and K. Domen, *J. Mater. Chem. A*, 2018, **6**, 15265–15273.

65 S. Bai, M. Cao, Y. Jin, X. Dai, X. Liang, Z. Ye, M. Li, J. Cheng, X. Xiao, Z. Wu, Z. Xia, B. Sun, E. Wang, Y. Mo, F. Gao and F. Zhang, *Adv. Energy Mater.*, 2014, **4**, 1301460.

66 K. Sun, N. Park, Z. Sun, J. Zhou, J. Wang, X. Pang, S. Shen, S. Y. Noh, Y. Jing, S. Jin, P. K. L. Yu and D. Wang, *Energy Environ. Sci.*, 2012, **5**, 7872–7877.